Biophysical Journal Volume 98 February 2010 606–616

Microarchitecture Is Severely Compromised but Motor Protein Function Is Preserved in Dystrophic *mdx* Skeletal Muscle

O. Friedrich,[†§*] M. Both,[†] C. Weber,[†] S. Schürmann,[†] M. D. H. Teichmann,[†] F. von Wegner,[†¶] R. H. A. Fink,[†] M. Vogel,[‖] J. S. Chamberlain,[††] and C. Garbe[‡]

[†]Medical Biophysics, Institute of Physiology and Pathophysiology, and [‡]Interdisciplinary Center for Scientific Computation, Ruprecht Karls University, Heidelberg, Germany; [§]School of Biomedical Sciences, University of Queensland, Brisbane, Australia; [¶]Brain Imaging Center, Johann Wolfgang Goethe University, Frankfurt, Germany; [‖]Center for Nanoscale Systems, Harvard University, Cambridge, Massachusetts; and [††]Department of Neurology, University of Washington, Seattle, Washington

ABSTRACT Progressive force loss in Duchenne muscular dystrophy is characterized by degeneration/regeneration cycles and fibrosis. Disease progression may involve structural remodeling of muscle tissue. An effect on molecular motorprotein function may also be possible. We used second harmonic generation imaging to reveal vastly altered subcellular sarcomere microarchitecture in intact single dystrophic *mdx* muscle cells (~1 year old). Myofibril tilting, twisting, and local axis deviations explain at least up to 20% of force drop during unsynchronized contractile activation as judged from cosine angle sums of myofibril orientations within *mdx* fibers. In contrast, in vitro motility assays showed unaltered sliding velocities of single *mdx* fiber myosin extracts. Closer quantification of the microarchitecture revealed that dystrophic fibers had significantly more Y-shaped sarcomere irregularities ("verniers") than wild-type fibers (~130/1000 μm^3 vs. ~36/1000 μm^3). In transgenic mini-dystrophin-expressing fibers, ultrastructure was restored (~38/1000 μm^3 counts). We suggest that in aged dystrophic toe muscle, progressive force loss is reflected by a vastly deranged micromorphology that prevents a coordinated and aligned contraction. Second harmonic generation imaging may soon be available in routine clinical diagnostics, and in this work we provide valuable imaging tools to track and quantify ultrastructural worsening in Duchenne muscular dystrophy, and to judge the beneficial effects of possible drug or gene therapies.

INTRODUCTION

Duchenne muscular dystrophy (DMD) is the most common inherited muscle disease. Although promising new gene therapy concepts have been developed in animal models, a cure for humans is still not available. The pathophysiology of the dystrophin deficiency in DMD muscle that leads to progressive weakness and a reduced lifespan remains puzzling. Dystrophin provides mechanical stability (1), but is also involved in Ca^{2+} signaling and ion channel function (2–7). Studies in human DMD myotubes and adult dystrophic *mdx* mouse muscle fibers revealed complex events triggered by a lack of dystrophin, including persistent inflammation, regeneration/degeneration cycles, aberrant mechanotransduction, and Ca^{2+} or ion channel dysregulation (6,8–12). Indeed, membrane fragility-associated myoplasmic Ca^{2+} overload in dystrophic muscle is known to trigger proteolytic (13) and proinflammatory pathways (10,14), and sustained inflammation may be a driving force for muscle degeneration, necrosis, and fibrotic tissue replacement (15). A striking feature of *mdx* muscle is gross morphological cellular alterations, i.e., fiber branching and deformities, due to degeneration and hastened incomplete regeneration (16). After dystrophic onset in *mdx* mice (~3–6 weeks old (17)), the occurrence of branched fibers steadily increases with age (16). Although such fibers were first described more than 15 years ago, the question of how the dystrophic process affects myofibril or sarcomere geometry remains elusive, mainly because of the limited resolution of conventional light microscopy (16) and the difficulty of obtaining a single-fiber three-dimensional (3D) structure from histological sections. It is important to understand the dystrophic process because it is well established that force output in dystrophic muscle (18,19), and particularly in branched fibers, is reduced (20). This force decrement progresses with age (21,22) and worsens with exercise (23), and a deranged micromorphology could greatly account for ongoing disease symptoms.

Recent developments in multiphoton microscopy have made it possible to perform minimally invasive, highly selective imaging of myosin in muscle cells with the use of nonlinear second harmonic generation (SHG) techniques (24,25). SHG microscopy has been used to visualize sarcomeres in various animal models (26), in patient muscle biopsies (26,27), and even in vivo in humans (28). However, a quantitative 3D analysis of sarcomere microarchitecture in single dystrophic muscle fibers is still lacking. For use in future clinical settings, it would be desirable to have image algorithms at hand to extract sensitive structural parameters with which to monitor the beneficial effects of drug treatment or gene therapy on a micrometer scale.

Given the chronic inflammatory nature of muscular dystrophy (14,29), one can speculate that gross

Submitted June 30, 2009, and accepted for publication November 5, 2009.

*Correspondence: oliver.friedrich@physiologie.uni-heidelberg.de or o.friedrich@uq.edu.au

M. Vogel's present address is Dept. of Molecular Neurogenetics, Max Planck Institute of Biophysics, Frankfurt, and Concert Medical Optics, Rauenberg, Germany.

O. Friedrich is both first and senior author.

Editor: K. W. Ranatunga.

0006-3495/10/02/0606/11 $2.00

doi: 10.1016/j.bpj.2009.11.005

morphological alterations in aged muscle should also be reflected in the microarchitecture of the muscle. Unfortunately, there is only sparse information available on whether a lack of dystrophin also alters motorprotein function (30,31). Here, we performed 3D SHG microscopy in intact single muscle fibers from wild-type (wt), dystrophic *mdx*, and transgenic *mdx* mice expressing mini-dystrophin (MinD). We developed automated imaging algorithms to locate and count local striation pattern disruptions. These were vastly increased in *mdx* muscle, but almost restored to wt levels in MinD muscle. We also extracted local angle cosine sum profiles through single fibers, which showed that misorientations from adjacent myofibrils could account for force detriments in *mdx* fibers. Lastly, in vitro motility assays of single muscle fiber myosin extracts showed similar filament sliding velocities among strains. Therefore, the dystrophic process results in remodeling of the muscle microarchitecture without affecting molecular motorprotein interactions.

MATERIALS AND METHODS

Single-fiber preparation, SHG imaging, and in vitro motility assays

For details regarding the materials and methods used in this work, see Methods S1 in the Supporting Material.

Quantitative image analysis: automated tool to count sarcomere irregularities

SHG images of muscle fibers may show local deviations from the usual perfectly alternating sarcomere pattern, with some appearing as Y-shaped structures (sometimes called ''verniers'' (25,32); see Discussion). To quantify such verniers, we developed an imaging algorithm in the MATLAB environment (The MathWorks, Natick, MA). First, noise was reduced by adaptive Wiener filtering. Applying the boundary tensor (33) to stacks, signal phase φ, direction ψ, and energy E were extracted. The boundary tensor was computed from polar, separable filters defined in the Fourier domain. The width of radial parts in Fourier space was kept constant for all data sets ($\sigma = 6$), but the filters were tuned for the dominant frequency of sarcomeres. Depending on the image resolution, this frequency parameter f (40–120, arb. units) can easily be optimized by Fourier spectrum analysis of images. Apart from f, only the energy signal E threshold needs to be adapted to the data. This was chosen by visually inspecting the segmentation of fibers versus background. For different sets, this parameter ranged from 90 to 650 depending on the magnification and signal/noise ratio. The gradient $\nabla\psi$ of the direction map was computed from a Sobel filter optimized for directional isotropy (34). Areas with local deviations from the striation pattern were segmented by thresholding $\nabla\psi$. The threshold τ was initially optimized by comparing the outcome of ''by-eye detection'' with the algorithm on random slices. Individual verniers were detected by multiplying segmented areas with a binary map derived by segmentation of φ. Next, dilation and erosion operations with 3×3 or 5×5 disks (depending on image magnification) were used to discard spurious pixels outside the fibers. Finally, labeling was performed on binary images to count patches equivalent to verniers. Their pixel count N was computed from the thresholded energy signal E of the boundary tensor. The criterion for counting a detected patch as a vernier was a minimum number of connected pixels. This was correlated with verniers detected by eye and depended on the image magnifications, e.g., for a 0.12 μm XY voxel size, a ~25 pixel containing a patch accounting for a ~0.4 μm^2 structure area was judged as a vernier. The number of counts was given per fiber cross-sectional area in each slice or integrated to fiber volume units.

To check the reliability of the automated detection, segmented images were compared with raw images that had been manually marked for obvious sarcomere irregularities ''by eye'' by one of the observers not using the image algorithms. The criterion by eye was to mark areas with Y-like deformities. The sets were then compared with the outcome of the automated sequences. Although the algorithm does not follow verniers in the *z*-direction, and thus one count may reappear in adjacent slices when the verniers extend in *z*, this does not compromise our count profiles through fibers. Also, since the step size is the same throughout, any potential systematic error will not affect our comparative approach.

Myofibrillar orientations and summed angles of axis deviation to estimate overall force output

The overall force was estimated from myofibrillar orientation deviations in individual images. The mean orientation was computed as the mean direction $\underline{\psi}$ of the boundary tensor. The relative direction ψ_{rel} was then computed as $\psi_{rel} = \underline{\psi} - \psi + \pi$ (π was added to avoid problems in subsequent analyses from the discontinuity between 0 and 2π). As a measure of overall force F, the cosine sum over ψ_{rel} was normalized to the pixel count of visible sarcomere structures ($F = 1/N\,\Sigma \cos(\psi_{rel})$). This measure is one if all myofibrils are aligned, and approaches zero for orientations perpendicular to the main fiber axis.

RESULTS

SHG imaging of microarchitecture in aged wt, *mdx*, and MinD single muscle fibers

Fig. 1 shows the benefits of multiphoton SHG imaging in single fibers to reveal morphological abnormalities. Although single fibers from adult *mdx* mice show apparent macroscopic branching, the axial resolution of conventional light microscopy is poor and prevents a detailed 3D reconstruction. In contrast, single fibers expressing a Δ17-48 MinD show a normal, regular striation pattern. From these images, however, one cannot readily extrapolate that microstructure is intact. SHG microscopy (Fig. 1 *B*) is suitable for resolving the sarcomere pattern due to a nonlinear optical frequency-doubling effect specific for myosin (25,26), i.e., myosin rods (35,36). Using this setup, we were able to obtain images of sarcomere structure in *mdx* fibers (Fig. 1 *B*). We recorded SHG images through the whole fiber with a constant *z*-step of 0.3 μm for detailed 3D rendering. In striking contrast to wt fibers, the morphological deformities extend deep into the fiber center in *mdx* fibers. The 12-month-old *mdx* fiber in Fig. 2 is branched but also shows vastly twisted myofibrils arranged almost perpendicularly to the fiber axis. 3D rendering in this fiber (Fig. 2 *A*, *a–e*) and others (Fig. 2 *A*, *f*) reveals the whole extent of the deformed microarchitecture (see Movie S1). All *mdx* fibers showed central areas void of signal due to central nuclei (27). Fig. 2 *B* shows images of a branched *mdx* fiber's sarcomere and membrane pattern after sequential recording of SHG and two-photon di-8-ANEPPS (2 μM) fluorescence. Two planes ~4 μm apart are shown. Obviously, the fascicle with sarcomeres at abnormal angles is fully covered by membrane that is continuous with the main fiber body. Therefore, such fascicles sticking out of the fiber belong to the same syncytia. This shows that such branches are not an artifact resulting from enzymatic

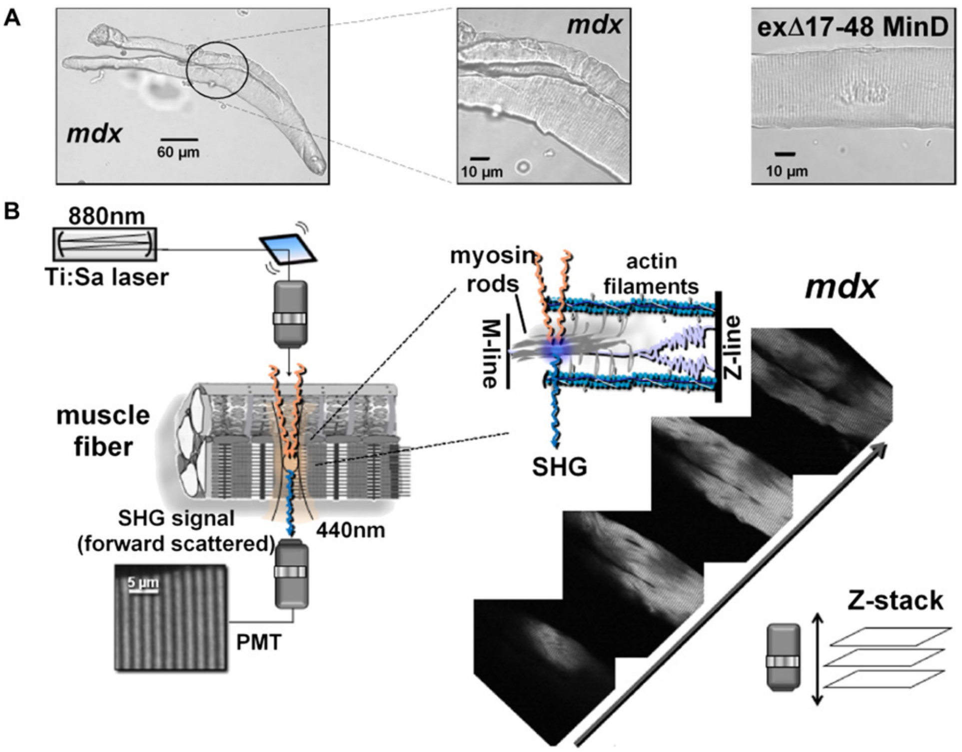

FIGURE 1 SHG imaging in single muscle fibers. (*A*) Transillumination single-fiber images only reflect gross morphological alterations in *mdx* fibers that are not present in Δ17-48 MinD fibers. (*B*) The setup for in situ SHG microscopy. Intrinsic SHG signals from myosin obtained with a pulsed laser allow optical sectioning of microarchitecture in intact single fibers without the need to introduce external dyes. The forward-scattered SHG signal is collected by a nondescanned photomultiplier tube.

isolation. Fig. 2 *B*, *d*, shows a magnified di-8-ANEPPS image and its overlay with the SHG signal from another *mdx* fiber near a branching point. Both signals do not colocalize. Also, the di-8-ANEPPS profile shows the well-known tubular double-row pattern of mammalian muscle, confirming correct localization of both signals.

Sarcomere lattice disruptions (i.e., verniers) are vastly increased in *mdx* but restored to normal quantities in MinD fibers

A closer look at larger magnifications of the SHG sections reveals myofibrillar disturbances of the regular sarcomere pattern, with some appearing as Y-shaped structures. In wt muscle, such deformities are mostly located at the fiber periphery (Fig. 3 *A*), whereas *mdx* fibers show an abundance of irregularities extending deep into the fiber center (Fig. 3, *A* and *G*). Of interest, in transgenic MinD fibers, these are also still present in the middle parts of cells but in much lower numbers, in more similarity to wt fibers. Those images suggest that the number of local deviations from the regular sarcomere pattern could be a measure of the degree of altered microarchitecture in aged *mdx* fibers. The nomenclature for these structures is inconclusive. They may represent local striation disruptions resulting from unaligned myofibrils, sarcomere deformities within one fibril, or local hypercontractions. For the sake of simplicity, we refer to them as verniers (25,32) (see Discussion).

To automatically determine the number and localization of verniers in a fiber volume, we used an automated imaging algorithm (Fig. 3 *B*), which proved to be very reliable in comparison with detection by eye. The comparison in Fig. 3 *F* shows a normalized manual count of 4.14/100 μm^2 versus an automated count of 5.31/100 μm^2. In another slice ~5.5 μm below the plane shown, the counts were 4.62/100 μm^2 and 4.94/100 μm^2. In randomly selected sections from five other *mdx* fibers, the manual versus automated counts (per 100 μm^2 fiber area) were as follows: 2.54 vs. 3.21, 7.90 vs. 2.98, 3.77 vs. 4.02, 3.47 vs. 2.18, and 5.38 vs. 7.66. In *mdx* single fibers, the vernier numbers were markedly increased throughout cross-sectional areas, whereas they were very low in wt fibers (Fig. 3, *C–E*). In MinD fibers (Fig. 3, *C* and *D*), they were more prominent at fiber edges but declined to almost wt levels through the fiber. 3D reconstructions of segmented verniers within the SHG volume showed streaks of lattice shifts running through central parts of fiber branches in *mdx* muscle (Fig. 3 *G*). This is shown for an *mdx* fiber with the SHG signal subsequently removed from the overlay volume (fiber with two branches in Fig. 3 *G, c–e*; see Movie S2). The volume count for this fiber was 160/1.000 μm^3. Detected verniers from all sections integrated to the fiber volume confirmed significantly larger numbers in *mdx* compared to wt fibers. Of interest, transgenic expression of MinD completely prevented dystrophic microarchitecture with counts similar to wt fibers (Fig. 3 *E*; $P < 0.01$).

Complex myofibril deformations reflect a smaller force output due to misorientated force vectors in *mdx* muscle

The deformed 3D structure is compatible with a reduced isometric force output in *mdx* fibers. Sarcomeres would act

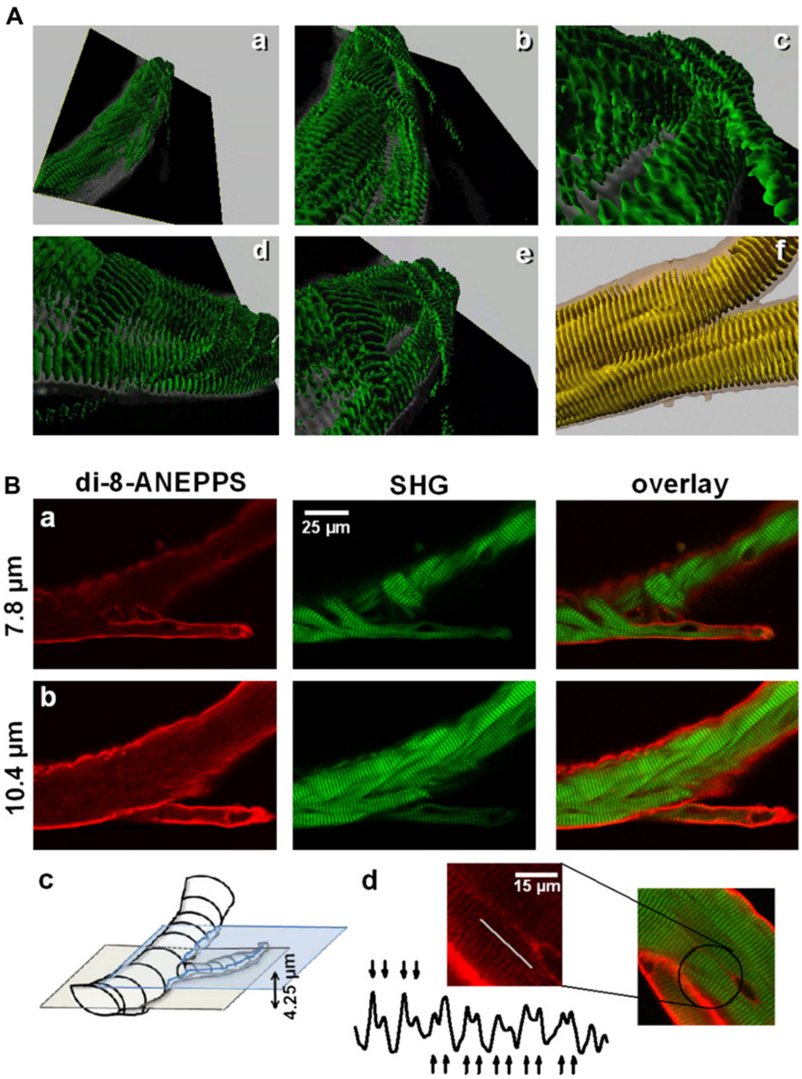

FIGURE 2 SHG imaging in single *mdx* fibers reveals a vastly deranged microarchitecture. (*A*) 3D reconstruction from SHG *z*-stacks through an intact single *mdx* fiber (~12 months) with macroscopic fiber branching reveals deformations (myofibril twisting, tilting, and marked local axis deviations) spreading throughout the cell (*a–e*). Panel *f* shows a different *mdx* fiber with myofibril tilting (see Movie S1). (*B*) Co-imaging of two-photon di-8-ANEPPS fluorescence and SHG shows that the fascicle with abnormal sarcomere angles sticking out of the main trunk is fully covered by membrane, lying inside the syncytia (*a* and *b* are ~4 μm apart in the *z*-direction within the fiber; *c*, sketch; *d*, larger magnification of a different *mdx* fiber near a branching area showing the tubular double-row pattern (di-8-ANEPPS, *red*) that does not colocalize with the SHG signal (*green*)).

in an unsynchronized manner due to different myofibril orientations along the axis. This is also suggested by individual force vectors drawn by eye into a SHG image of an *mdx* fiber (Fig. 4 *A*). To estimate the degree of myofibrillar angle misalignment, we integrated over local angle distributions in each optical slice by summing all cosine values from the direction-filtered images and normalized them to the fiber area. Fig. 4 *B* shows examples from one wt and two *mdx* fibers with either branching or multiple myofibril twisting. The SHG image of one optical plane and the corresponding relative angle distribution images are shown. In the latter, the angle direction is normalized to the long fiber axis, yielding high-bit entries when the fibrils run along the long fiber axis and low entries when they run almost perpendicular to it. In the wt fiber shown, all myofibrils run along the fiber axis. Fig. 4 *D* summarizes the *z*-distributions from normalized cosine averages of *z*-stack images as in Fig. 4 *B*. The cosine sum is close to unity throughout the whole stack in wt, but is clearly reduced in *mdx* fibers. In MinD fibers, the cosine angle sums were similar to wt (not shown), documenting that MinD expression prevented dystrophic architecture. This result is a very first approximation to the force drop directly derived from micromorphology in intact single *mdx* toe fibers (~1 year old).

In vitro motility assays of single-fiber extracts from wt, *mdx*, and MinD muscles

The morphological results presented above show that contractile activation of dystrophic muscle at ~1 year of age should already be compromised simply due to biophysical considerations. To test whether the advanced dystrophic process in such fibers also affects motorprotein function per se, we performed in vitro motility assays of single-fiber myosin extracts (Fig. 5 *A*) (37). Fig. 5 *B* shows images taken from a time series (10 fps) that contains numerous moving filaments tracked in time. A postimaging analysis (38) yields a sliding velocity distribution profile with representative examples given for each strain (Fig. 5 *C*). The Gaussian profiles in each of the strains are very similar. When we compared the median velocities v_u from several fiber extracts at two temperatures (~27°C and ~31°C), we detected no

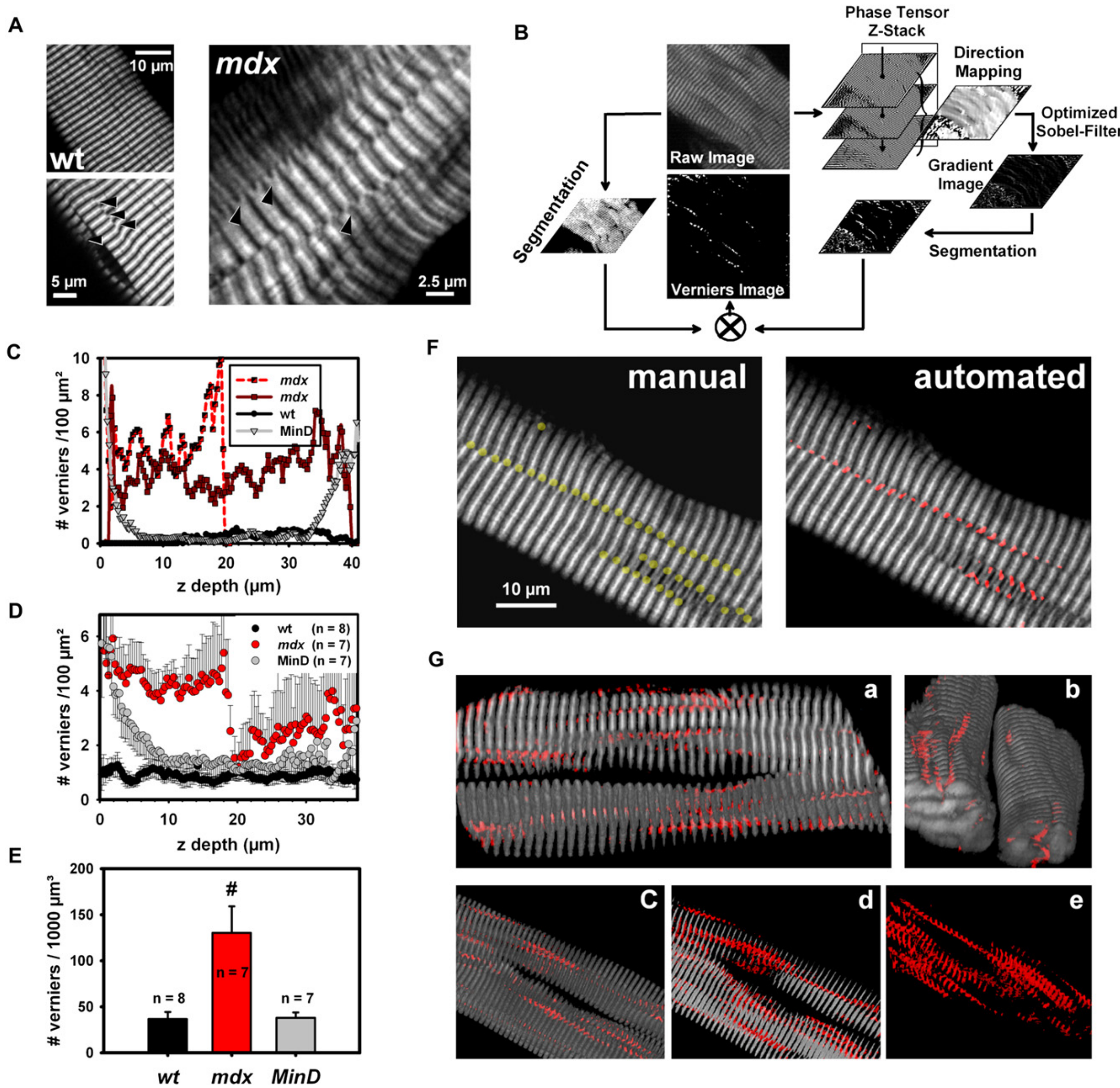

FIGURE 3 Quantification of local sarcomere irregularities in single wt, *mdx*, and MinD fibers. (*A*) SHG images from a single wt fiber show Y-shaped misalignments (''verniers''; see Discussion) at the periphery (automated counts: 0 in the upper, 11 in the lower wt image). In *mdx* fibers, these are abundant and extend deep into the fiber center (counts: 35 in the *mdx* image). (*B*) Overview of the image analysis algorithm applied to single-fiber SHG *z*-stacks to extract slice-wise and volume-integrated local vernier counts (*C–E*). (*C*) Fiber area normalized counts through the *z*-stack in sample wt, *mdx* (a thin fiber and one with diameter similar to wt and MinD fibers), and MinD fibers. (*D*) Mean vernier distributions in several fibers. (*E*) Volume-integrated counts. Vernier counts are increased severalfold in *mdx* fibers and reduced to wt levels in MinD fibers. (*F*) Comparison of vernier counts detected by eye with automated analysis shows reliable detection (manual: 44, automated: 42 counts). (*G*) 3D reconstruction of overlaid stacks from SHG signal (*gray*) and detected verniers (*red*) in a branched *mdx* fiber (*a–e*). Subsequent removal of the SHG signal intensity from the volume reveals continuous vernier streaks running mostly through central fiber parts (*c–e*; see Movie S2). Count for this fiber: 160/1000 μm^3. *: $P < 0.05$.

significant difference. We did not investigate lower temperatures because at such temperatures, more and more filaments remained stationary in the assay. Taken together, the results show that although the microarchitecture is deranged in adult *mdx* toe muscle, the dystrophic process does not affect isolated actomyosin interactions.

DISCUSSION

Dystrophic DMD or *mdx* skeletal muscle presents with early onset of weakness associated with impaired Ca^{2+} handling (9,39,40) and aberrant mechanosensitive pathways (7,11,41). It is believed that these events trigger chronic inflammation or reactive oxygen species production (8,10,14,29), which

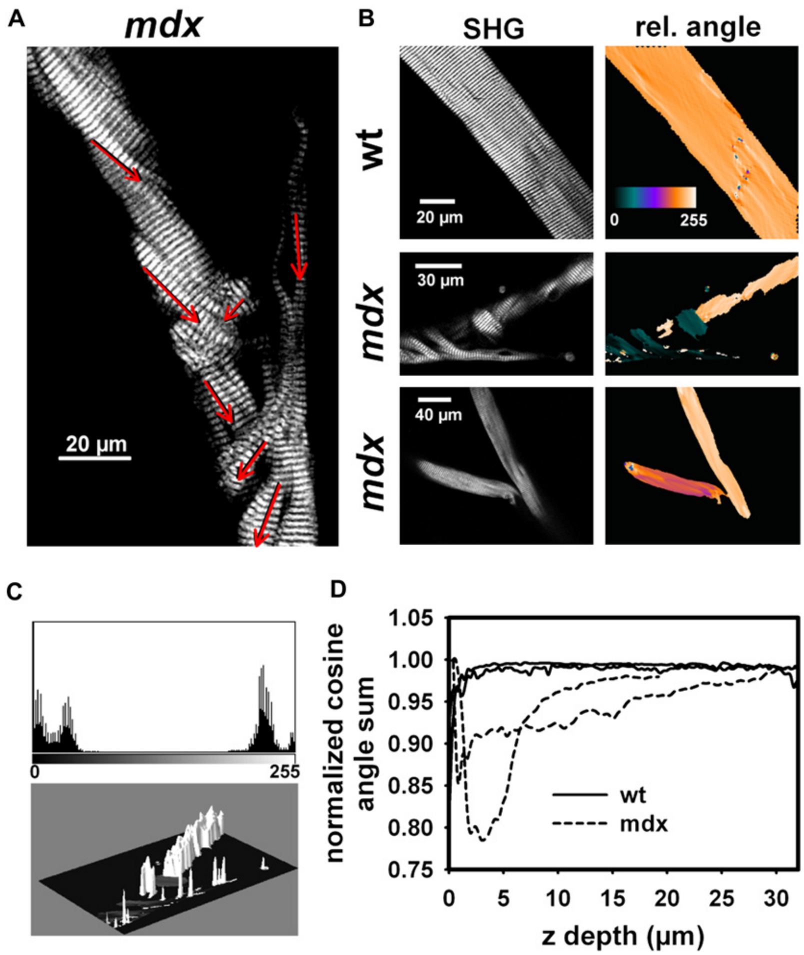

FIGURE 4 Myofibrillar local axis deviations visualized by SHG predict reduced force output in *mdx* muscle fibers. (*A*) SHG section of a single *mdx* fiber with local deviations from the long axis. ''By eye'' drawing of local force vectors suggests a reduced sum force vector. (*B*) SHG images from one wt fiber and two *mdx* fibers, and relative angle images derived from direction-filtered segments. High-pixel entries: local relative angle parallel to the long fiber axis. (*C*) Pixel histogram and surface plot of *mdx* fiber in *B*. (*D*) Normalized cosine angle sum profiles in two wt and two *mdx* fibers show values close to unity in wt fibers, but much smaller values within *mdx* fibers.

sustain the degenerative cycles. In *mdx* mice, massive degeneration occurs at ~3–6 weeks, followed by regeneration (17). Furthermore, *mdx* muscle shows progressive weakness and deterioration with age (21,22), morphologically branched or deformed fibers, atrophies, and spontaneous clusters of ''revertant'' fibers (6,21), a consequence of ongoing fiber regeneration (21,42). The abnormal morphology in *mdx* muscle is believed to be due to disruptions in muscle growth/regeneration programs (41,43). Thus, although the *mdx* mouse has a milder phenotype than DMD patients, it is still an excellent model for studying the pathology of muscular dystrophy (44,45) and the efficacy of targeted dystrophin replacement via gene delivery strategies.

Progressive muscle weakness in *mdx* muscle is paralleled by exhaustive regeneration and grossly altered macromorphology of fibers from animals >1 year of age (16,20,21), and we speculated that in aged muscle, abnormal microarchitecture rather than changes to molecular motorprotein function could account for the force decline in addition to altered Ca^{2+} homeostasis and mechanotransduction. We tested the hypothesis that subcellular myofibril patterns are disrupted in aged *mdx* muscle, but filament sliding velocities are unaffected. We reasoned that MinD is sufficient to rescue the *mdx* phenotype.

Single *mdx* muscle fiber syncytia: possible sources of a deranged cytoarchitecture

Gross morphological abnormalities in dystrophic *mdx* muscle, in both severely affected diaphragm (46) and mildly affected limb muscle (20,21), increase in frequency with age (16). Striking features seen with light or confocal microscopy are fiber branches/deformities (16,20,47). When judging ultrastructure in living cells, microscopy resolution and specificity for stained structures are crucial. Head et al. (16) recorded polarized light ''low power images'' of dissociated *mdx* muscle fibers showing multiple branches and fascicles, hypercontracted areas, or cytoplasmic bridges (16). Using confocal microscopy on fixed flexor digitorum brevis, extensor digitorum longus (edl), and soleus muscle blocks, they showed that such branches are not an artifact of enzymatic dissociation (16). We confirm that branches and fascicles are completely covered by membrane and are continuous with the main fiber trunk (Fig. 2 *B*). This also applies to another murine muscular dystrophy model, dy/dy, in which the laminin α-2 complex is mutated. Single fibers in dy/dy mice show similar deformities that constitute a single syncytia and not individual fibers closely associated with each other (48).

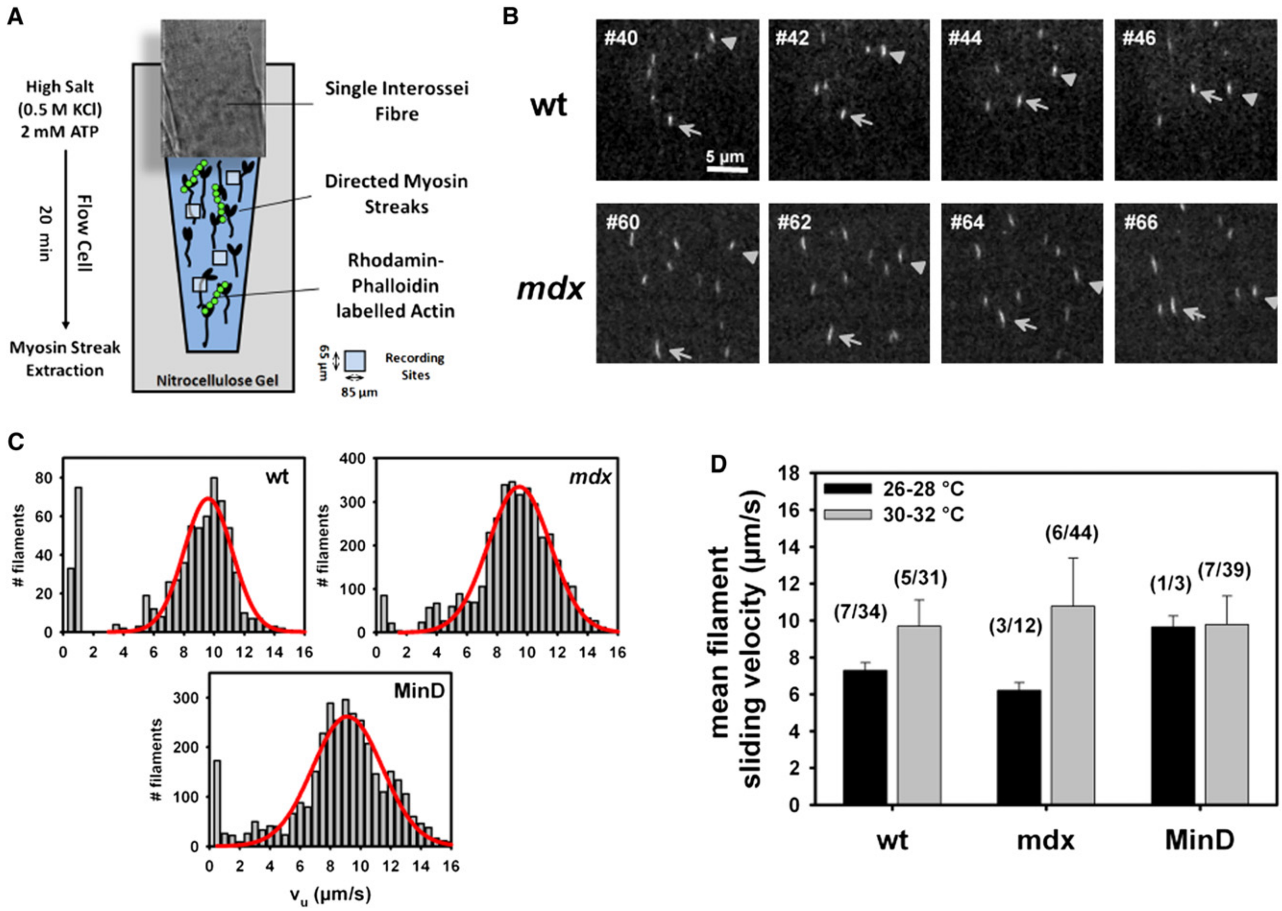

FIGURE 5 In vitro motility assay from single wt, *mdx*, and MinD fiber myosin extracts. (*A*) The setting used to extract myosin from single fibers for in vitro motility assays. (*B*) Selected images from a time series recorded in a single fiber extract of a wt and *mdx* muscle. Arrows and arrowheads point to one filament that is tracked through subsequent images. (*C*) Sliding velocity (v_u) distributions and (*D*) mean median v_u values (*n* recordings as in *B* from *m* single-fiber extracts) were similar in all strains.

Are such fiber deformities paralleled by disruptions in the membrane or cytoskeleton continuity? Using voltage-sensitive di-8-ANEPPS, Woods et al. (49) studied t-tubule properties in *mdx* muscle and found no altered tubular or sarcomere patterns in young animals (15 weeks old). However, a recent study revealed branching and displacement defects during embryogenesis, along with attrition of PAX-7 positive *mdx* myotubes (50), suggesting that morphological abnormalities are not only secondary to degeneration/regeneration but may also be due to a primary myogenesis defect associated with a lack of dystrophin. In a recent study on ~9-month-old *mdx* flexor digitorum brevis single fibers, Lovering et al. (41) confirmed our previous results on aberrant Ca^{2+} sparks after osmotic challenge (7). They reported no obvious alterations in cytoskeleton structure or membrane staining in bifurcating single cells; however, looking closely at their desmin and FM-464 images, one can readily observe areas of disrupted striation patterns, i.e., shifts in the myofibril lattice that would correspond to vernier images in our study (see their Fig. 3). Their subtle cytoskeleton alterations are seen in areas close to branches, but not exclusively, which would be in agreement with our findings. Moreover, Lovering et al. (41) only recorded single sections within a fiber, whereas we focused on complete *z*-stacks. It is reasonable to expect that the cytoskeleton and membrane have to follow sarcomere alterations throughout the fiber to maintain a functional syncytia. Therefore, our study presents (for the first time, to our knowledge) a detailed 3D view of deranged microarchitecture that might be missed when only single planes are examined.

Altered myofibrillar geometry is a feature of ongoing repetitive degeneration/regeneration cycles in dystrophic muscle (16,41,42,50). In *mdx* mice, chronic inflammation is present (14) that might impair ordered regeneration, resulting in the misalignment of newly formed myofibrils. Gene expression profiles revealed marked up-regulation of inflammatory proteins (e.g., Spp1 and S100a9), structural extracellular matrix, and sarcomere/cytoskeleton remodeling processes (51). Very recent evidence points to an involvement of the pleiotropic transcription factor NF-κB in inflammation-triggered failure of ordered regeneration in *mdx* muscle. Increased metalloproteinase-9 (MMP-9) levels cause dystrophic myopathy, and in vivo blockade of NF-κB in *mdx* mice blocks MMP-9 expression and augments skeletal muscle regeneration (52). Future studies will need to assess whether the ultrastructural changes presented in this study can be prevented by antiinflammatory treatment.

Myofibril architecture in single intact *mdx* fibers established by 3D SHG microscopy

SHG signals originate from myosin, and thus SHG microscopy provides an easy means to study myofibril and sarcomere patterns in healthy and diseased muscle (35,36). Using SHG, we confirmed morphological alterations in aged single *mdx* muscle fibers seen with other optical methods (16,20,41,48). Apart from branching, the myofibrils were vastly tilted and twisted. This was especially visible in 3D reconstructions. To our knowledge, complete *z*-stacks of dystrophic fibers, obtained with either SHG or confocal microscopy, have not been reported before. Thus, the severity of myofibril derangement in aged *mdx* muscle fibers may have gone unnoticed up to now because 1), conventional light microscopy does not allow detailed 3D reconstruction of fiber morphology; and 2), in most confocal or SHG studies, the focus was on muscle from young animals that were not yet showing massive regeneration-related structural abnormalities (26,47). In another study on tissue sections (rather than single fibers), a more wavy SHG pattern was observed in muscle from young (5-week-old) *mdx* mice (26) in which necrosis was present, but before the effective regeneration phase (>5 weeks (16,17)). The degree of morphological malformation in an individual fiber reflects its history of mechanical demand, stress, and damage, and thus the degeneration/regeneration cycles can differ among muscles. It is almost impossible to assess the history of limb muscles in an animal, which may account for some of the differences in the literature on *mdx* muscle fiber architecture (41,48).

Reduced force in *mdx* fibers derived from integrated myofibril orientations

From a biophysical standpoint, myofibril misorientations in single *mdx* fibers can partly explain the decreased force in *mdx* muscle because neighboring sarcomere activation would be unsynchronized. Our image analysis gives the first quantitative estimate (to our knowledge) of an ultrastructure-related force deficit in *mdx* fibers. This deficit may vary among individual fibers, depending on the degree of myofibril twisting and local angle deviations. The force deficit is also inhomogeneous within fibers, depending on whether additional branches are present or not (Fig. 4). We found normalized cosine angle deviations of up to 20% from the long axis that would not contribute to force output. Our current image processing does not yet include the *z*-aspect of myofibril tilting that would additionally contribute to the overall force deficit. Ongoing work in our laboratory will include *z*-segmentation and individual myofibril *z*-tracking. However, our force deficit profiles in single fibers are in good agreement with experimental results. Williams et al. (47) found a 10–20% reduced Ca^{2+} activated isometric force in fast-twitch skinned fibers from adult (17- to 23-week-old) soleus and edl *mdx* muscles. In young (3- to 6-week-old) *mdx* mice, force deficits were significant in fast-twitch portions of the soleus, and even slightly larger in the edl. However, the young age group is not yet associated with substantial morphological deformities and probably reflects alterations in Ca^{2+} handling during early necrosis (post) necrotic phase (16). Lynch et al. (22) found a significantly reduced isometric specific peak force in ~17-month-old *mdx* edl muscle, accounting for ~80% of the values found for wt (22). One can imagine that contractile activation of misoriented myofibrils (Fig. 2) would even worsen the situation of large membrane stress (53), producing local membrane tears or disrupting membrane integrity in *mdx* muscle. In a study of skinned fibers, it was found that branch points were weaker than nonbranched portions of dystrophic fibers, such that deformed fibers would eventually break at the branch points when submaximally activated (48). Thus, it is reasonable to speculate that the altered microarchitecture we see in single *mdx* fibers would add substantially to increased fiber susceptibility and maintain inflammation during disease progression. Moreover, therapeutic approaches will probably not be able to completely correct muscular dystrophy at later stages when the phenotype becomes ''morphologically fixed''. Chronic regeneration in DMD differs from regeneration after a single damage event. In a previous study, early regeneration after acute muscle damage in rats produced asynchronous repair events by days 3–5, but architecture was restored after 3 weeks (54). Early gene therapy in DMD might overcome the problem of persistent morphological alterations, and, indeed, one of the major findings in our study is that single transgenic *mdx* fibers expressing MinD show normal regular patterns similar to wt fibers. This clearly shows that MinD not only restores many alterations on the membrane, ion channel, and excitation-contraction coupling level (5,7,46), it also preserves muscle architecture, presumably by preventing myofibrillar remodeling during chronic inflammation in *mdx* muscle (51).

An automated tool to quantify sarcomere patterns: *mdx* microarchitecture is resuscitated by transgenic expression of MinD

When we analyzed sarcomere patterns more closely in SHG stacks, we observed abundant areas of adjacently misaligned myofibrils in *mdx* fibers that appeared as shifts in the strictly alternating sarcomere pattern, producing Y-shaped structures. Such an ultrastructure was previously observed in skeletal muscle fibers by SHG (25–27) or conventional microscopy under various conditions, most of which related myofibrillar irregularities to damage/regeneration cycles (54,55). For example, quadriceps muscle samples from patients with chronic knee joint damage showed myofibrillar disintegration and disrupted striations after surgical repair, but a restored ultrastructure after completed rehabilitation (55). Irregular sarcomere patterns were also observed in a strenuous chronic weight-lifting exercise rat model (56), and sarcomere and *z*-line deformities were revealed in electron microscopy images of crustacean muscle during claw regeneration (57). Finally, desmin is essential for myofibril integrity with myofibrillar branching in $\text{Des}^{-/-}$ knockout mice (58).

Some of the Y-shaped structures in our SHG images can be called verniers according to early descriptions in light microscopy studies of human skeletal muscle (32). Verniers are local differences in the striation pattern frequency between adjacent myofibrils, such that the lattice appears unsynchronized. Verniers can be a result of misaligned myofibrils or local hypercontractions (53,59). Sarcomere splittings that also occur in $\text{Des}^{-/-}$ muscle (58), or staircase-like patterns in 3D reconstructions in normal muscle due to myofibril helicoids (25,32) do not strictly reflect verniers. Our imaging algorithm detects structures with local angular deviations. It can detect most Y-shaped structures, but it cannot further classify their origin. For the sake of simplicity, we refer to detected counts as verniers, although we are aware that some of them may not represent true verniers (which, however, does not affect our comparative approach). SHG images of wt muscle showed only a few verniers, mostly located at the fiber periphery. They probably are the result of newly formed myofibrils that were incorporated at the periphery during regeneration in normal muscle. Similarly to muscle in Pompe's disease (27), *mdx* fibers showed abundant verniers that extended deep into the fiber center. In transgenic MinD fibers, verniers were still present in the central parts, but the numbers were more similar to those observed in wt fibers. These results suggest that verniers can provide an adequate measure for monitoring disease progression or therapeutic success in future clinical trials, as SHG microscopy is potentially applicable to patients in vivo (28).

Molecular actomyosin interaction is unaltered in dystrophic muscle

The molecular function of myosin isolated from *mdx* muscle can give insight into whether the dystrophic process projects down to the motorprotein level or not. This is important to know because it is the logical consequence of our morphology data, which already suggest a compromised force output on a biophysical basis, and can help determine whether impaired motorprotein function per se is also part of the dystrophic process. If so, such a mechanism should probably be secondary to dystrophic deterioration, as dystrophin is unlikely to interact directly with myosin. Our motility assay yielded almost identical velocity profiles for all strains, and median velocities v_u were not significantly different. This shows that the cross-bridge kinetics is unaltered by the dystrophic process, and the reduced force in *mdx* muscle probably involves upstream mechanisms, i.e., excitation-contraction coupling (6,9–12), and morphological microstructure alterations (the latter at least for the age group and muscle type examined in this study).

A previous motility assay on diaphragm muscle from 9-month-old *mdx* mice revealed significantly slower actomyosin sliding velocities compared to wt (31). Also, in a very recent study, Canepari et al. (30) found significantly slower actin sliding velocities for myosin type IIB extracted from 6-month-old *mdx* gastrocnemius muscle, but no difference for type I myosin extracts from soleus single fibers. One difference between their results and ours may stem from the fact that they used pure myosin isoforms from single fibers to rule out contributions from slower myosin isoforms in hybrid fibers. Such ''contaminations'' can slow down average velocities even if only small quantities of slow myosin are present (60). Even though we did not fiber type for myosin isoforms, we think our results are solid because 1), we recently only detected myosin type IIA isoforms in homogenates from interossei muscles of the strains (61); and 2) fiber-type switching occurs in aging *mdx* limb muscles, thus reducing type IIB and increasing type I isoforms (30). Even if there were a slow isoform ''contamination'' in our myosin IIA containing *mdx* interossei extracts, a much faster sliding velocity for fast myosin would be expected in *mdx* muscle, which was not observed (30). Of interest, and in agreement with this argument, even though Coirault et al. (31) found slower velocities in *mdx* diaphragm, there was no difference compared to wt for *mdx* semitendinosus muscle containing type IIB myosin in 9-month-old animals (31). This controversy may, therefore, reflect unchanged type IIA properties that have not been studied by other groups and/or that the extent of muscle damage in *mdx* muscle is relevant for myosin function, especially in type IIB isoforms (31,41). More research is needed to address this point, as well as the age dependence of various *mdx* muscle myosins. However, in agreement with our results, a previous study (61) found that the unloaded speed of shortening was similar in intact *mdx*, wt, and MinD interossei fibers.

SUPPORTING MATERIAL

Methods and two movies are available at http://www.biophysj.org/biophysj/supplemental/S0006-3495(09)01728-7.

This study was supported in part by the German Ministry for Education and Research (13N7871 to R.H.A.F.); Landesforschungsschwerpunkt Baden Württemberg (to R.H.A.F.); Australian Research Council International Fellowship (to O.F.); Center of Nanoscale Systems, Harvard University; and National Nanotechnology Infrastructure Network (to M.V. under National Science Foundation cooperative agreement 0335765). M.D.H.T. was a scholar of the German National Merit Foundation.

REFERENCES

1. Consolino, C. M., and S. V. Brooks. 2004. Susceptibility to sarcomere injury induced by single stretches of maximally activated muscles of *mdx* mice. *J. Appl. Physiol.* 96:633–638.

2. Gailly, P. 2002. New aspects of calcium signaling in skeletal muscle cells: implications in Duchenne muscular dystrophy. *Biochim. Biophys. Acta*. 1600:38–44.
3. Yeung, E. W., S. I. Head, and D. G. Allen. 2003. Gadolinium reduces short-term stretch-induced muscle damage in isolated *mdx* mouse muscle fibres. *J. Physiol.* 552:449–458.
4. Whitehead, N. P., E. W. Yeung, and D. G. Allen. 2006. Muscle damage in *mdx* (dystrophic) mice: role of calcium and reactive oxygen species. *Clin. Exp. Pharmacol. Physiol.* 7:657–662.
5. Friedrich, O., M. Both, …, R. H. Fink. 2004. Mini-dystrophin restores L-type calcium currents in skeletal muscle of transgenic *mdx* mice. *J. Physiol.* 555:251–265.
6. Friedrich, O., F. von Wegner, …, P. Rohrbach. 2008. L-type Ca^{2+} channel function is linked to dystrophin expression in mammalian muscle. *PloS One*. 3:e1762.
7. Teichmann, M. D. H., F. V. Wegner, …, O. Friedrich. 2008. Inhibitory control over Ca(2+) sparks via mechanosensitive channels is disrupted in dystrophin deficient muscle but restored by mini-dystrophin expression. *PLoS One*. 3:e3644.
8. Gervásio, O. L., N. P. Whitehead, …, D. G. Allen. 2008. TRPC1 binds to caveolin-3 and is regulated by Src kinase—role in Duchenne muscular dystrophy. *J. Cell Sci.* 121:2246–2255.
9. DiFranco, M., C. E. Woods, …, J. L. Vergara. 2008. Dystrophic skeletal muscle fibers display alterations at the level of calcium microdomains. *Proc. Natl. Acad. Sci. USA*. 105:14698–14703.
10. Acharyya, S., S. A. Villalta, …, D. C. Guttridge. 2007. Interplay of IKK/NF-κB signaling in macrophages and myofibers promotes muscle degeneration in Duchenne muscular dystrophy. *J. Clin. Invest.* 117:889–901.
11. Kumar, A., N. Khandelwal, …, A. M. Boriek. 2004. Loss of dystrophin causes aberrant mechanotransduction in skeletal muscle fibers. *FASEB J.* 18:102–113.
12. Imbert, N., C. Vandebrouck, …, C. Cognard. 2001. Calcium currents and transients in co-cultured contracting normal and Duchenne muscular dystrophy human myotubes. *J. Physiol.* 534:243–255.
13. Gailly, P., F. De Backer, …, J. M. Gillis. 2007. In situ measurements of calpain activity in isolated muscle fibres from normal and dystrophin-lacking *mdx* mice. *J. Physiol.* 582:1261–1275.
14. Messina, S., D. Altavilla, …, G. Vita. 2006. Lipid peroxidation inhibition blunts nuclear factor-κB activation, reduces skeletal muscle degeneration, and enhances muscle function in *mdx* mice. *Am. J. Pathol.* 168:918–926.
15. Peterson, J. M., and D. C. Guttridge. 2008. Skeletal muscle diseases, inflammation, and NF-κB signaling: insights and opportunities for therapeutic intervention. *Int. Rev. Immunol.* 27:375–387.
16. Head, S. I., D. A. Williams, and D. G. Stephenson. 1992. Abnormalities in structure and function of limb skeletal muscle fibres of dystrophic *mdx* mice. *Proc. R. Soc. Lond.* 248:163–169.
17. Tanabe, Y., K. Esaki, and T. Nomura. 1986. Skeletal muscle pathology in X chromosome-linked muscular dystrophy (*mdx*) mouse. *Acta Neuropathol.* 69:91–95.
18. Yoshimura, M., M. Sakamoto, …, S. Takeda. 2004. AAV vector-mediated microdystrophin expression in a relatively small percentage of *mdx* myofibers improved the *mdx* phenotype. *Mol. Ther.* 10:821–828.
19. Dellorusso, C., R. W. Crawford, …, S. V. Brooks. 2001. Tibialis anterior muscles in *mdx* mice are highly susceptible to contraction-induced injury. *J. Muscle Res. Cell Motil.* 22:467–475.
20. Chan, S., S. I. Head, and J. W. Morley. 2007. Branched fibers in dystrophic *mdx* muscle are associated with a loss of force following lengthening contractions. *Am. J. Physiol. Cell Physiol.* 293:C985–C992.
21. Pastoret, C., and A. Sebille. 1995. *mdx* mice show progressive weakness and muscle deterioration with age. *J. Neurol. Sci.* 129:97–105.
22. Lynch, G. S., R. T. Hinkle, …, J. A. Faulkner. 2001. Force and power output of fast and slow skeletal muscles from *mdx* mice 6–28 months old. *J. Physiol.* 535:591–600.
23. De Luca, A., S. Pierno, …, D. Conte Camerino. 2003. Enhanced dystrophic progression in *mdx* mice by exercise and beneficial effects of taurine and insulin-like growth factor-1. *J. Pharmacol. Exp. Ther.* 304:453–463.
24. Vanzi, F., M. Capitanio, …, F. S. Pavone. 2006. New techniques in linear and non-linear laser optics in muscle research. *J. Muscle Res. Cell Motil.* 27:469–479.
25. Both, M., M. Vogel, …, D. Uttenweiler. 2004. Second harmonic imaging of intrinsic signals in muscle fibers in situ. *J. Biomed. Opt.* 9:882–892.
26. Plotnikov, S. V., A. M. Kenny, …, W. A. Mohler. 2008. Measurement of muscle disease by quantitative second-harmonic generation imaging. *J. Biomed. Opt.* 13:044018.
27. Ralston, E., B. Swaim, …, N. Raben. 2008. Detection and imaging of non-contractile inclusions and sarcomeric anomalies in skeletal muscle by second harmonic generation combined with two-photon excited fluorescence. *J. Struct. Biol.* 162:500–508.
28. Llewellyn, M. E., R. P. J. Barretto, …, M. J. Schnitzer. 2008. Minimally invasive high-speed imaging of sarcomere contractile dynamics in mice and humans. *Nature*. 454:784–788.
29. Hnia, K., J. Gayraud, …, D. Mornet. 2008. L-arginine decreases inflammation and modulates the nuclear factor-κB/matrix metalloproteinase cascade in *mdx* muscle fibers. *Am. J. Pathol.* 172:1509–1519.
30. Canepari, M., R. Rossi, …, R. Bottinelli. 2009. Actin sliding velocity on pure myosin isoforms from dystrophic mouse muscles. *Muscle Nerve*. 40:249–256.
31. Coirault, C., F. Lambert, …, Y. Lecarpentier. 2002. Velocity of actomyosin sliding in vitro is reduced in dystrophic mouse diaphragm. *Am. J. Respir. Crit. Care Med.* 165:250–253.
32. Tiegs, O. W. 1934. Observations on the structure of striated muscle fibre. *Proc. R. Soc. Lond. B Biol. Sci.* 116:38–54.
33. Köthe, U. 2003. Integrated edge and junction detection with the boundary tensor. *Proc. 9th Int. Conf. Comput. Vis.*, Nice. 1:424–431.
34. Scharr, H., S. Körkel, and B. Jähne. 1997. Numerische Isotropieoptimierung von FIR-Filtern mittels Querglättung. Proc. DAGM-Symposium Mustererkennung. Springer-Verlag, Berlin. 367–374.
35. Plotnikov, S. V., A. C. Millard, …, W. A. Mohler. 2006. Characterization of the myosin-based source for second-harmonic generation from muscle sarcomeres. *Biophys. J.* 90:693–703.
36. Schürmann, S., C. Weber, …, M. Vogel. 2007. Myosin rods are the source of second harmonic generation signals in skeletal muscle. *Proc. SPIE*. 6442:64421U.
37. Höök, P., and L. Larsson. 2000. Actomyosin interactions in a novel single muscle fiber in vitro motility assay. *J. Muscle Res. Cell Motil.* 21:357–365.
38. von Wegner, F., T. Ober, …, M. Vogel. 2008. Velocity distributions of single F-actin trajectories from a fluorescence image series using trajectory reconstruction and optical flow mapping. *J. Biomed. Opt.* 13:054018.
39. Bellinger, A. M., S. Reiken, …, A. R. Marks. 2009. Hypernitrosylated ryanodine receptor calcium release channels are leaky in dystrophic muscle. *Nat. Med.* 15:325–330.
40. Robert, V., M. L. Massimino, …, T. Pozzan. 2001. Alteration in calcium handling at the subcellular level in *mdx* myotubes. *J. Biol. Chem.* 276:4747–4755.
41. Lovering, R. M., L. Michaelson, and C. W. Ward. 2009. Malformed *mdx* myofibers have normal cytoskeletal architecture yet altered EC coupling and stress-induced Ca^{2+} signaling. *Am. J. Physiol. Cell Physiol.* 297:C571–C580.
42. Yokota, T., Q. L. Lu, …, T. A. Partridge. 2006. Expansion of revertant fibers in dystrophic *mdx* muscles reflects activity of muscle precursor cells and serves as an index of muscle regeneration. *J. Cell Sci.* 119:2679–2687.
43. Grounds, M. D. 1998. Age-associated changes in the response of skeletal muscle cells to exercise and regeneration. *Ann. N. Y. Acad. Sci.* 854:78–91.

44. Banks, G. B., and J. S. Chamberlain. 2008. The value of mammalian models for Duchenne muscular dystrophy in developing therapeutic strategies. *Curr. Top. Dev. Biol.* 84:431–453.
45. Chamberlain, J. S., J. Metzger, …, J. A. Faulkner. 2007. Dystrophin-deficient *mdx* mice display a reduced life span and are susceptible to spontaneous rhabdomyosarcoma. *FASEB J.* 21:2195–2204.
46. Decrouy, A., J. M. Renaud, …, B. J. Jasmin. 1997. Mini-dystrophin gene transfer in mdx4cv diaphragm muscle fibers increases sarcolemmal stability. *Gene Ther.* 4:401–408.
47. Williams, D. A., S. I. Head, …, D. G. Stephenson. 1993. Contractile properties of skinned muscle fibres from young and adult normal and dystrophic (*mdx*) mice. *J. Physiol.* 460:51–67.
48. Head, S. I., D. G. Stephenson, and D. A. Williams. 1990. Properties of enzymatically isolated skeletal fibres from mice with muscular dystrophy. *J. Physiol.* 422:351–367.
49. Woods, C. E., D. Novo, …, J. L. Vergara. 2005. Propagation in the transverse tubular system and voltage dependence of calcium release in normal and *mdx* mouse muscle fibres. *J. Physiol.* 568:867–880.
50. Merrick, D., L. K. J. Stadler, …, J. Smith. 2009. Muscular dystrophy begins early in embryonic development deriving from stem cell loss and disrupted skeletal muscle formation. *Dis. Model. Mech.* 2:374–388.
51. Turk, R., E. Sterrenburg, …, P. A. ’t Hoen. 2006. Common pathological mechanisms in mouse models for muscular dystrophies. *FASEB J.* 20:127–129.
52. Li, H., A. Mittal, …, A. Kumar. 2009. Matrix metalloproteinase-9 inhibition ameliorates pathogenesis and improves skeletal muscle regeneration in muscular dystrophy. *Hum. Mol. Genet.* 18:2584–2598.
53. Suchyna, T. M., and F. Sachs. 2007. Mechanosensitive channel properties and membrane mechanics in mouse dystrophic myotubes. *J. Physiol.* 581:369–387.
54. Politi, P. K., S. Havaki, …, G. Lyritis. 2006. Bupivacaine-induced regeneration of rat soleus muscle: ultrastructural and immunohistochemical aspects. *Ultrastruct. Pathol.* 30:461–469.
55. Lańcut, M., P. Godlewski, …, K. Czerny. 2004. Investigations of ultrastructure of damaged and regenerated skeletal muscle fibers. *Ann. Univ. Mariae Curie Sklodowska [Med].* 59:80–85.
56. Ho, K. W., R. R. Roy, …, R. E. Carrow. 1980. Skeletal muscle fiber splitting with weight-lifting exercise in rats. *Am. J. Anat.* 157:433–440.
57. West, J. M., D. C. Humphris, and D. G. Stephenson. 1995. Characterization of ultrastructural and contractile activation properties of crustacean (*Cherax destructor*) muscle fibres during claw regeneration and moulting. *J. Muscle Res. Cell Motil.* 16:267–284.
58. Li, Z., M. Mericskay, …, D. Paulin. 1997. Desmin is essential for the tensile strength and integrity of myofibrils but not for myogenic commitment, differentiation, and fusion of skeletal muscle. *J. Cell Biol.* 139:129–144.
59. Huxley, A. F., and R. E. Taylor. 1958. Local activation of striated muscle fibres. *J. Physiol.* 144:426–441.
60. Harris, D. E., S. S. Work, …, D. M. Warshaw. 1994. Smooth, cardiac and skeletal muscle myosin force and motion generation assessed by cross-bridge mechanical interactions in vitro. *J. Muscle Res. Cell Motil.* 15:11–19.
61. Friedrich, O., C. Weber, …, R. H. Fink. 2008. Unloaded speed of shortening in voltage-clamped intact skeletal muscle fibers from wt, mdx, and transgenic minidystrophin mice using a novel high-speed acquisition system. *Biophys. J.* 94:4751–4765.